

Microscopic calculation of proton and alpha-particle inelastic scattering to study the excited states of ${}^6\text{He}$ and ${}^8\text{He}$

Yoshiko Kanada-En'yo

Department of Physics, Kyoto University, Kyoto 606-8502, Japan

Kazuyuki Ogata

Research Center for Nuclear Physics (RCNP), Osaka University, Ibaraki 567-0047, Japan

Department of Physics, Osaka City University, Osaka 558-8585, Japan and

Nambu Yoichiro Institute of Theoretical and Experimental Physics (NITEP), Osaka City University, Osaka 558-8585, Japan

Elastic and inelastic cross sections of the $p + {}^6\text{He}$, $p + {}^8\text{He}$, and $\alpha + {}^8\text{He}$ reactions were investigated using the Melbourne g -matrix folding approach with the theoretical densities of ${}^6\text{He}$ and ${}^8\text{He}$ obtained by a microscopic structure model of antisymmetrized molecular dynamics (AMD). Microscopic coupled-channel (MCC) calculations of the $p + {}^6\text{He}$ and $p + {}^8\text{He}$ reactions were performed to investigate transition properties of the ${}^6\text{He}(2_1^+)$ and ${}^8\text{He}(2_1^+)$ states. The MCC+AMD calculations reproduced elastic cross sections of the $p + {}^6\text{He}$ reaction at $E = 40.9$ MeV/A and of the $p + {}^8\text{He}$ reaction at $E = 32.5$ and 72 MeV/A, which have both been measured by inverse kinematics experiments. For $p + {}^6\text{He}$ inelastic scattering to the 2_1^+ state, the calculated result was in reasonable agreement with the (p, p') data at $E = 24.5$ and 40.9 MeV/A and supported the AMD prediction of the neutron transition matrix element $M_n = 7.9$ fm². For the $p + {}^8\text{He}$ inelastic scattering to ${}^8\text{He}(2_1^+)$, the MCC+AMD calculation overshot the (p, p') cross sections at $E = 72$ MeV/A by a factor of three. According to a phenomenological model analysis, M_n values in the range of 4–6 fm² were favored to reproduce the ${}^8\text{He}(2_1^+)$ cross sections of the $p + {}^8\text{He}$ reaction at $E = 72$ MeV/A. For the $\alpha + {}^8\text{He}$ reaction, the MCC+AMD calculation reproduced the elastic cross sections at $E = 26$ MeV/A. Theoretical predictions of the (p, p') and (α, α') cross sections to the ${}^8\text{He}(0_2^+)$, ${}^8\text{He}(1_1^-)$, ${}^8\text{He}(2_3^+)$ and ${}^8\text{He}(3_1^-)$ states are also given.

I. INTRODUCTION

Elastic and inelastic (p) cross sections have been extensively measured for various stable nuclei to investigate the density of the ground states and the transition profiles of nuclear excitations. Because of their higher sensitivity of the p scattering to the neutron part, the (p, p') data for $Z \neq N$ stable nuclei have often been used to determine the neutron transition matrix elements M_n , as the counterparts to electric probes for the proton transition matrix elements M_p . Additionally, the (α, α') reaction is an alternative tool that can be used to observe the isoscalar component of low-lying nuclear excitations as well as isoscalar giant resonances (e.g., see Refs. [1–4] and the refs. therein). Because of the existence of high-quality beams, precise data on the p and α scattering are available for various stable nuclei in wide ranges of incident energies. To investigate the isoscalar and isovector components of 2^+ excitations, the neutron-proton ratio M_n/M_p of $E2$ transitions has been previously evaluated using a combination of γ -decay and the inelastic scattering data on different probes including e , p , α , and π^+/π^- , for a wide range of mass numbers [5–9]. Over the years, α inelastic scattering experiments have also been used as a probe to cluster states in $Z = N$ nuclei, such as those of ${}^{12}\text{C}$ and ${}^{16}\text{O}$ [10–13].

For unstable nuclei, pion and electron scattering experiments are not practical. Instead, the p scattering off unstable nuclei has generally been investigated by experiments using inverse kinematics. The amount of p elastic and inelastic scattering data, which provides useful in-

formation on the structure of unstable nuclei, is rapidly increasing. Further, α scattering experiments for unstable nuclei have also been achieved using inverse kinematics [14–16].

On the theoretical side, describing the existing (p, p') and (α, α') data with reaction calculations is an urgent issue for the study of excited states of target nuclei. For analyses of inelastic scattering, phenomenological reaction models, such as distorted wave Born approximation (DWBA), are often performed by adjusting nucleon–nucleus and nucleus–nucleus potentials to elastic scattering data. Such phenomenological tuning, which usually depends on the incident energy and the target nuclei, requires a significant amount of elastic scattering data. However, for unstable nuclei, data are available only for limited energy and angle ranges and are not as high-quality as data on stable nuclei. Given this limit, the development of a microscopic reaction model, that does not rely on system- and energy-dependent tuning is necessary.

For experimental and theoretical studies of p scattering off unstable nuclei, microscopic reaction approaches using the g -matrix folding model have been developed. These approaches are suitable for our purpose because the energy dependence and medium effects are taken into account in the effective g -matrix nucleon–nucleon (NN) interaction, which is derived from a realistic NN force based on the Brueckner theory. For studies on the p inelastic scattering, the Jeukenne-Lejeune-Mahaux (JLM) interaction [17] has often been used as an effective g -matrix NN interaction and has been applied to micro-

scopic calculations of (p, p') reactions for unstable nuclei including He, Li, Be, and C isotopes, along with microscopic structure calculations of the target nuclei [18–25].

Since the 1990s, experimental studies of $p + {}^6\text{He}$ and $p + {}^8\text{He}$ reactions have been widely performed (see the review in Ref. [23]). To extract information about the ground and 2_1^+ states via (p, p) and (p, p') reactions, respectively, a systematic analysis using JLM has been performed using the diagonal and transition densities of ${}^6\text{He}$ and ${}^8\text{He}$ obtained using theoretical structure models. $p + {}^6\text{He}$ inelastic scattering has also been investigated using a four-body calculation with a continuum discretized coupled channel considering the higher-order effects of continuum coupling with all 0^+ , 1^- , and 2^+ partial waves [25]. In principle, the g -matrix folding approach should not contain adjustable parameters, but JLM reaction calculations require phenomenological parameter tuning to fit the elastic data, which is usually performed by introducing renormalization factors of potentials.

Along a similar line to the microscopic reaction approaches, the Melbourne group has developed a microscopic folding model with an improved g -matrix NN interaction and demonstrated its success in reproducing p +nucleus elastic scattering for a wide range of target mass numbers and incident energies [26]. The Melbourne g -matrix folding approach has been widely tested for p and α elastic scattering, and the framework has also been successfully applied to inelastic processes [26–38]. Since the approach with the Melbourne g -matrix NN interaction has no adjustable parameters, it is a useful tool to test the reliability of structure inputs without model ambiguity on the reaction side. Because of its merit, one can directly access the structural properties of the ground and excited states via p scattering.

In this study, we investigated the elastic and inelastic cross sections of the $p + {}^6\text{He}$, $p + {}^8\text{He}$, and $\alpha + {}^8\text{He}$ reactions with the Melbourne g -matrix folding approach using the densities of ${}^6\text{He}$ and ${}^8\text{He}$ obtained by a structure model of antisymmetrized molecular dynamics (AMD) [39–41]. In the present calculations, we adopted the same framework of the reaction approach as in Refs. [35–38]. Namely, we used the folding model with a simplified treatment of the exchange term of the optical potential and multiple scattering theory [42] for p scattering and applied the approximation of an extended version of the nucleon–nucleus folding model for α scattering.

For the structural calculation using the AMD framework, the proton and neutron components of the diagonal and transition densities of ${}^6\text{He}$ and ${}^8\text{He}$ were microscopically obtained. Using the AMD densities, the microscopic coupled-channel (MCC) calculations of the $p + {}^6\text{He}$ and $p + {}^8\text{He}$ reactions were performed. Using this MCC+AMD model, the $p + {}^6\text{He}$, $p + {}^8\text{He}$, and $\alpha + {}^8\text{He}$ reactions can be investigated on the same footing. We first checked the ability of the MCC+AMD calculations to reproduce elastic cross sections by comparison with the (p, p) data and then investigated the transition properties of the ${}^6\text{He}(2_1^+)$ and ${}^8\text{He}(2_1^+)$ states via the (p, p') cross

sections. The $\alpha + {}^8\text{He}$ elastic and inelastic cross sections were also calculated using the MCC+AMD model, and the results were compared with the (α, α) data observed at $E = 72$ MeV/A. Further, theoretical predictions of the inelastic cross sections to the ${}^8\text{He}(0_2^+)$, ${}^8\text{He}(1_1^-)$, and ${}^8\text{He}(3_1^-)$ states were made.

The rest of the study is organized as follows. In Sec. II, the reaction model using the Melbourne g -matrix folding approach is explained. In Sec. III, the AMD calculation of the structures of the He isotopes is described. Sec. IV presents the results of the $p + {}^6\text{He}$ reaction, and Sec. V discusses the $p + {}^8\text{He}$ scattering to the ${}^8\text{He}(0_1^+)$ and ${}^8\text{He}(2_1^+)$ states. The calculated results of the $p + {}^8\text{He}$ and $\alpha + {}^8\text{He}$ scattering to higher excited states are shown in Sec. VI. Finally, a summary is given in Sec. VII.

II. REACTION MODEL: MELBOURNE g -MATRIX FOLDING APPROACH

The reaction calculations of p and α scattering were performed using the Melbourne g -matrix folding model approach, as in Refs. [35–38].

The nucleon–nucleus potentials were calculated by folding the Melbourne g -matrix NN interaction with the diagonal and transition densities of target nuclei, which were microscopically obtained by AMD. The Melbourne g -matrix interaction is an effective NN interaction in a nuclear medium and is based on a bare NN interaction of the Bonn B potential [43]. The α –nucleus potentials were obtained by folding the nucleon–nucleus potentials with an α density of a Gaussian form. In the present calculation, the spin-orbit term of the p –nucleus potentials was not taken into account to avoid complexity. It should be noted that the spin-orbit interaction can smear the dip structure of elastic cross sections, but it gives a minor contribution to absolute peak amplitudes at incident energies lower than $E_p = 100$ MeV except for at backward angles. For the details of the present reaction model, see Refs. [35–38] and the refs. therein.

III. STRUCTURE CALCULATIONS AND PROPERTIES OF ${}^6\text{He}$ AND ${}^8\text{He}$

A. AMD calculations

For use in MCC calculations, the diagonal and transition densities of the target nuclei were calculated using the AMD wave functions of ${}^6\text{He}$ and ${}^8\text{He}$, which were obtained in a previous study of He isotopes [44]. We used the wave functions labeled as “m56” and “v58”, which represented two choices of parametrization given in Table 1 of Ref. [44]. In this study, we call the former AMDm56 and the latter AMDv58. The details of the calculation procedures and the ground state structures of ${}^6\text{He}$ and ${}^8\text{He}$ were described in the previous work. It should be stressed that the AMD is a microscopic structure model

that considers the degrees of freedom of all the nucleons. Even though the model does not assume any clusters, α -like cluster structures with valence neutrons were obtained by the AMD calculation for low-lying ${}^6\text{He}$ and ${}^8\text{He}$ states.

In the present structure calculation, we used the basis AMD configurations obtained in the previous calculation but improved the accuracy of the numerical integration of the angular momentum projection to calculate the diagonal and transition densities of the excited states with high accuracy precision. Using the updated wave functions, we perform a diagonalization of the Hamiltonian and norm matrices and recalculated the structural properties including the energies, radii, and transition strengths.

B. Properties of the 0_1^+ and 2_1^+ states of ${}^6\text{He}$ and ${}^8\text{He}$

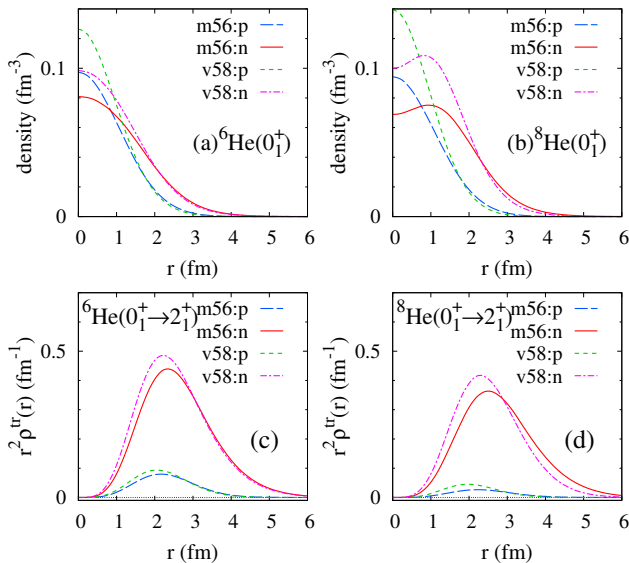


FIG. 1: Diagonal and transition densities calculated using AMDm56 and AMDv58. Proton and neutron components of the diagonal densities for (a) ${}^6\text{He}(0_1^+)$ and (b) ${}^8\text{He}(0_1^+)$ and those of the $0_1^+ \rightarrow 2_1^+$ transition densities for (c) ${}^6\text{He}$ and (d) ${}^8\text{He}$. The r^2 -weighted transition densities are plotted.

The structural properties of ${}^6\text{He}$ and ${}^8\text{He}$ are summarized in Table I. The calculated values of the root-mean-square (rms) point-proton and point-neutron radii of the ground state, 2_1^+ energies, and the proton and neutron components of the $0_1^+ \rightarrow 2_1^+$ transition matrix elements of ${}^6\text{He}$ and ${}^8\text{He}$ are shown together with the experimental radii and energies. The proton and neutron components of the diagonal and transition densities are shown in Fig. 1. In both the AMDm56 and AMDv58 results, the proton density remained in the inner region, whereas the neutron density was distributed in the outer region

indicating a neutron halo structure in ${}^6\text{He}(0_1^+)$ and a neutron skin structure in ${}^8\text{He}(0_1^+)$, which are generated by loosely bound valence neutrons around the α core. The AMDm56 and AMDv58 results were qualitatively similar but the AMDv58 results showed smaller radii than the AMDm56 results for ${}^8\text{He}$ in particular. As shown in Fig. 1(b), the AMDv58 results also showed a weaker neutron skin than did the AMDm56 results (Fig. 1(b)). This interaction dependence is regarded as an ambiguity of the structure calculation using the AMD model.

For the $0_1^+ \rightarrow 2_1^+$ transition, a remarkable neutron dominance was obtained in both the ${}^6\text{He}$ and ${}^8\text{He}$ systems. This neutron dominance in the ${}^6\text{He}(2_1^+)$ and ${}^8\text{He}(2_1^+)$ excitations is a general phenomenon in proton-closed nuclei with $N > Z$ and is caused by valence neutrons around a core, as seen in ${}^{18}\text{O}$. The neutron transition densities demonstrated a single-peak structure at the nuclear surface, as shown in Figs. 1(c) and (d).

To reveal the structure model ambiguity with respect to the proton and neutron densities, we compared the AMD results with several other calculations. In Table I, we show the theoretical values obtained by the stochastic variational calculation [51] and the no-core shell model (NCSM) calculations from Refs. [52–54]. For ${}^6\text{He}$, we also show the radii and transition matrix elements for a halo-type density set of the NCSM-based halo-type diagonal density (ρ_{halo}) and the 2pF-Tassie transition density ($\rho_{\text{Tassie}}^{\text{tr}}$) from Ref. [23]. All of the models gave qualitatively similar results with respect to the halo and skin structures, but quantitative differences can be observed in the neutron radii particularly. Regarding the $0_1^+ \rightarrow 2_1^+$ transition properties, the NCSM calculation gave almost the same values of M_p and M_n as the AMD predictions for both the ${}^6\text{He}$ and ${}^8\text{He}$ systems.

C. Higher excited states of ${}^8\text{He}$

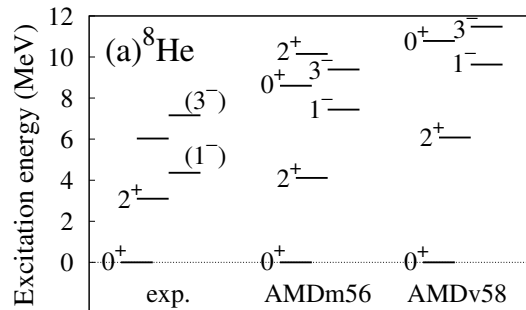


FIG. 2: Calculated energy spectra obtained by AMDm56 and AMDv58 and the experimental data from Ref. [50].

In Fig. 1, the calculated energy spectra of ${}^8\text{He}$, including the excited states above the 2_1^+ state are shown together with the experimental spectra. The calculated

TABLE I: Rms point-proton (R_p) and point-neutron (R_n) radii, 2_1^+ excitation energies (E_x), and proton (M_p) and neutron (M_n) components of the $0_1^+ \rightarrow 2_1^+$ transition matrix elements of ${}^6\text{He}$ and ${}^8\text{He}$. The results of AMDm56 and AMDv58 are shown together with the experimental data [45–50]. Theoretical values of other models, including those of the stochastic variational calculation [51], the NCSM calculation of Ref. [52] and that of Refs. [53, 54], are shown for comparison. In the rightmost column, the theoretical values of the halo-type density set of ρ_{halo} (NCSM-based halo-type diagonal density) and $\rho_{\text{Tassie}}^{\text{tr}}$ (2pF-Tassie transition density) for ${}^6\text{He}$ from Ref. [23] are shown. The experimental values of R_p were extracted from the charge radii [45, 46], and those of R_n were obtained from the R_p data and the empirical matter radii in Refs. [47, 48]. For NCSM[53, 54], the values of the NCSM($10\hbar\omega$) calculation of ${}^6\text{He}$ and those of the NCSM($v_{3\text{eff}}(4\hbar\omega)$) calculation of ${}^8\text{He}$ were taken from Ref. [23].

	Expt.	AMDm56	AMDv58	SVM	NCSM[52]	NCSM[53, 54]	halo-type[23]
${}^6\text{He}$							
R_p (fm)	1.92(1)	1.92	1.79	1.80	1.76(3)	1.76	2.03
R_n (fm)	2.39–2.77	2.48	2.39	2.67	2.55(10)	2.36	2.72
$E_x(2_1^+)$ (MeV)	1.80	1.4	2.0			2.63	
M_p (fm 2)		0.90	0.92			1.03	2.44
M_n (fm 2)		7.9	7.9			7.73	7.80
${}^8\text{He}$							
R_p (fm)	1.81(3)	1.92	1.69	1.71	1.74(6)	2.00	
R_n (fm)	2.60–2.75	2.63	2.33	2.53	2.60(10)	2.59	
$E_x(2_1^+)$ (MeV)	3.1(5)	4.1	6.1				
M_p (fm 2)		0.32	0.38			0.50	
M_n (fm 2)		7.6	6.4			6.67	

TABLE II: Excitation energies, rms radii, and M_p and M_n values of the $0_1^+ \rightarrow J^\pi$ transitions of ${}^8\text{He}$ calculated using AMDm56. The units for energy and radius are MeV and fm, respectively. The units for M_p and M_n for the IS0 and IS1 transitions are fm $^{\lambda+2}$, and those for the $E2$ and $E3$ transitions are fm $^\lambda$.

${}^8\text{He}(J^\pi)$	E_x	R_p	R_n	R_m		M_p	M_n
0_1^+	0.0	1.92	2.63	2.47			
0_2^+	8.6	2.12	3.10	2.89	IS0	0.51	2.8
2_1^+	4.1	1.98	2.78	2.60	$E2$	0.32	7.6
2_2^+	10.2	2.05	2.99	2.78	$E2$	-0.01	0.04
2_3^+	13.4	2.43	3.70	3.43	$E2$	0.30	4.5
1_1^-	7.4	2.08	3.30	3.04	IS1	-1.84	13.5
3_1^-	9.4	2.08	3.24	2.99	$E3$	-0.04	37

values of the proton, neutron, and matter radii of the ground and excited states, and the proton and neutron components of the transition matrix elements from the ground to excited states are listed in Table II. Similar to the ${}^8\text{He}(2_1^+)$ state, the ${}^8\text{He}(0_2^+)$, ${}^8\text{He}(1_1^-)$, ${}^8\text{He}(2_3^+)$, and ${}^8\text{He}(3_1^-)$ states also had neutron skin structures and neutron-dominant transitions, which again indicate the predominant contribution of valence neutrons around the α -like cluster. More details on the transition properties for these higher states are discussed in Sec. VI.

IV. $p + {}^6\text{He}$ SCATTERING

A. MCC+AMD results for $p + {}^6\text{He}$ cross sections

The $p + {}^6\text{He}$ reactions at $E = 24.5$ and 40.9 MeV/A were calculated using the MCC calculation with the AMDm56 and AMDv58 densities. The ${}^6\text{He}(0_1^+)$ and ${}^6\text{He}(2_1^+)$ states and all of the $\lambda = 0$ and $\lambda = 2$ transitions between them were taken into account. In addition to this 2ch(MCC) calculation, one-step cross sections were also calculated using the DWBA. In Fig. 3, the calculated $p + {}^6\text{He}$ cross sections are compared with experimental data observed in inverse kinematics [27, 28].

Fig. 3(a) shows the $p + {}^6\text{He}$ elastic cross sections. The MCC calculations using the AMDm56 and AMDv58 densities reasonably described the observed (p, p) data at $E = 24.5$ MeV/A and did a good job of reproducing the data at $E = 40.9$ MeV/A except for the dip structure, which could be improved by the smearing effect of the spin-orbit interaction omitted in the present calculation.

Unlike the AMDm56 results, the second peak of the cross section was shifted to backward angles in the AMDv58 results because of the smaller radii of ${}^6\text{He}(0_1^+)$, but there was not enough experimental data to select a better calculation. Compared with the DWBA (one-step) cross sections, the MCC calculation obtained a lower-amplitude second peak because of the coupled channel (CC) effect with the 2_1^+ state and showed better agreement with the (p, p) data at $E = 24.5$ MeV/A.

Fig. 3(b) shows the inelastic cross sections to the ${}^6\text{He}(2_1^+)$ state. In both the AMDm56 and AMDv58 results, the first-peak amplitude of the cross sections was in reasonable agreement with the data at $E = 24.5$ and 40.9 MeV/A, but the calculation did not satisfactorily describe the behavior of the angle dependence in detail. This result indicates that the neutron transition strength of the AMD prediction is a reasonable value.

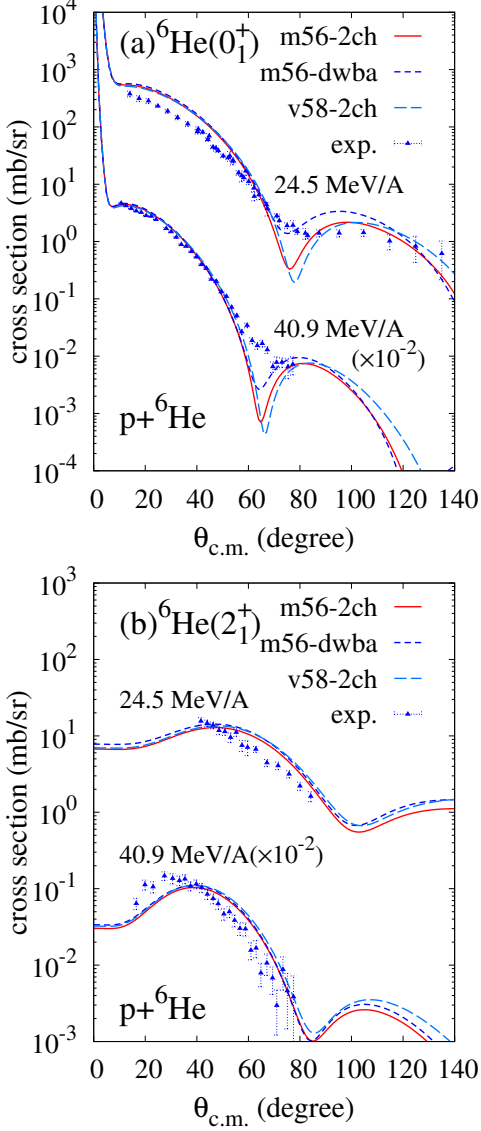


FIG. 3: Calculated ${}^6\text{He}(0_1^+)$ and ${}^6\text{He}(2_1^+)$ cross sections of the $p + {}^6\text{He}$ scattering at $E = 24.5$ MeV/A and $E = 40.9$ MeV ($\times 10^{-2}$) compared with the experimental data. The 2ch(MCC) calculations using AMDm56 and AMDv58 and the DWBA calculation using AMDm56 are shown. The experimental data at $E = 24.5, 25,$ and 25.7 MeV/A [28, 55, 56] and the data at $E = 40.9$ MeV/A ($\times 10^{-2}$) [27] are shown.

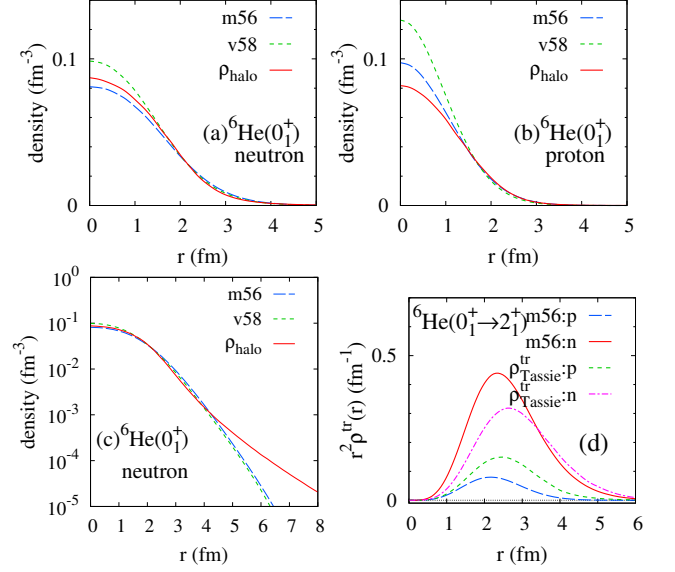


FIG. 4: Comparison of the densities of ${}^6\text{He}$ between the halo-type [23] and AMD densities. Panels (a) and (b) compare the neutron and proton components, respectively, of the NCSM-based halo-type diagonal density (ρ_{halo}) with the AMDm56 and AMDv58 diagonal densities. Panel (c) shows the neutron densities in log scale. In panel (d), the 2pF-Tassie transition density ($\rho_{\text{Tassie}}^{\text{tr}}$) of the $0_1^+ \rightarrow 2_1^+$ transition is compared with the AMDm56 and AMDv58 transition densities. The r^2 -weighted transition densities are also plotted. The data for ρ_{halo} are taken from Fig. 13 of Ref. [23], and those of $\rho_{\text{Tassie}}^{\text{tr}}$ are taken from Fig. 14 of Ref. [23].

B. Ambiguity of structure inputs: comparison with halo-type density

As previously mentioned, the present MCC+AMD results on the $p + {}^6\text{He}$ reaction were not satisfactory in their detailed description of the angle dependence of the ${}^6\text{He}(2_1^+)$ cross sections. As can be seen in Fig. 3(b), the calculation obtained a wider angle distribution than the observed cross sections at both energies of $E = 24.5$ and 40.9 MeV/A. This energy-independent trend may suggest that a modification of the AMD transition densities is necessary.

To investigate the ambiguity of the structure inputs, we performed a model analysis of the $p + {}^6\text{He}$ cross sections by adopting the halo-type density set of ρ_{halo} and $\rho_{\text{Tassie}}^{\text{tr}}$ presented in Ref. [23]. Note that $\rho_{\text{Tassie}}^{\text{tr}}$ is not a microscopic density but a phenomenological transition density given by a derivative form of ρ_{halo} , which was renormalized to reproduce the (p, p') data by a JLM reaction calculation in Ref. [23]. The proton component of $\rho_{\text{Tassie}}^{\text{tr}}$ was renormalized to fit $B(E2) = 3.1 \pm 0.6 e^2\text{fm}^4$, whereas the neutron component was tuned to reproduce the (p, p') data. Figs. 4(a)-(c) compare the halo-type diagonal density (ρ_{halo}) with the AMDm56 and AMDv58 diagonal densities of ${}^6\text{He}$. Compared with the AMDm56 and AMDv58 densities, the neutron component of ρ_{halo}

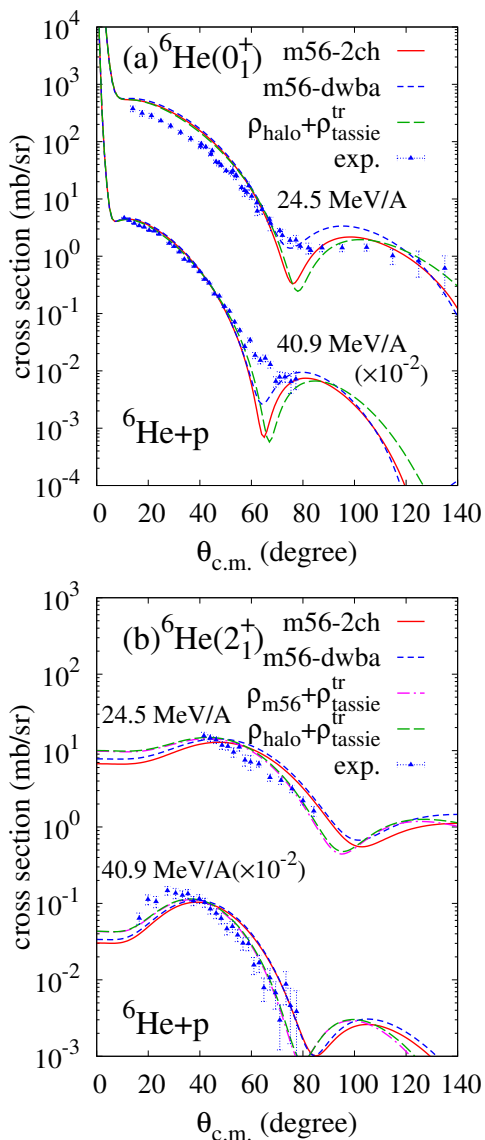


FIG. 5: Calculated ${}^6\text{He}(0_1^+)$ and ${}^6\text{He}(2_1^+)$ cross sections of the $p + {}^6\text{He}$ scattering at $E = 24.5$ MeV/A and $E = 40.9$ MeV ($\times 10^{-2}$) obtained with the AMDm56 densities and those obtained with the halo-type density set. The 2ch(MCC) and DWBA calculations with AMDm56, and the 2ch(MCC) calculations with ρ_{halo} (NCSM-based halo-type diagonal density) and $\rho_{\text{Tassie}}^{\text{tr}}$ (2pF-Tassie transition density) of ${}^6\text{He}$ from Refs. [23, 27]. The experimental data at $E = 24.5, 25, 25.7$ MeV/A [28, 55, 56] and the data at $E = 40.9$ MeV/A ($\times 10^{-2}$) [27] are also shown.

showed a long tail in the $r \geq 5$ fm region (Fig. 4(c)). In Fig. 4(d), a comparison of the halo-type transition density ($\rho_{\text{Tassie}}^{\text{tr}}$) with the AMDm56 transition density of ${}^6\text{He}$ is shown. The neutron component of $\rho_{\text{Tassie}}^{\text{tr}}$ shows a broader radial distribution compared with AMDm56 but gives almost the same neutron transition matrix element $M_n = 7.8$ fm² as AMDm56 ($M_n = 7.9$ fm²).

To see the sensitivity of the p scattering cross sections

to the ${}^6\text{He}$ densities, we calculated the $p + {}^6\text{He}$ reaction using the Melbourne g -matrix folding model with the halo-type densities. Fig. 5 shows a comparison of the results of the ${}^6\text{He}(0_1^+)$ and ${}^6\text{He}(2_1^+)$ cross sections between two sets of diagonal and transition densities, the halo-type density set (ρ_{halo} and $\rho_{\text{Tassie}}^{\text{tr}}$) and the AMDm56 density set. Note that the (p, p) cross sections were dominantly affected by the diagonal density of the ${}^6\text{He}(0_1^+)$ state, whereas the (p, p') cross sections to the ${}^6\text{He}(2_1^+)$ state were sensitive to the $0_1^+ \rightarrow 2_1^+$ transition density. As can be seen in Fig. 5(a), there was only a small difference in the (p, p) cross sections between the halo-type and AMDm56 density cases even though they had different tail behaviors in the neutron diagonal density. In the (p, p') cross sections to the ${}^6\text{He}(2_1^+)$ state, the absolute amplitude of the first peak was almost the same as each of the others, though the two calculations resulted in different angle dependences. In the halo-type density case, the peak amplitude of the ${}^6\text{He}(2_1^+)$ cross sections shifted to forward angles and the angle distribution was narrower than in the AMDm56 case because of the slightly broader neutron transition density (Fig. 4 (d)).

From this model analysis, it can be concluded that the angle dependence of the 2_1^+ cross sections was directly affected by the radial behavior of the neutron transition density. At the same time, the absolute amplitude of the first-peak cross sections was not sensitive to the detailed shape of the transition density but was determined by the transition matrix elements. The results obtained using the halo-type density set demonstrated better agreement with the (p, p') data, which may suggest that a broader neutron transition density than that of AMDm56 was favored. However, there remains some deviation from the data for the forward angles at $E = 40.9$ MeV/A. For an accurate description of the (p, p') data observed for the 2_1^+ resonance energy region, other effects such as coupling with the continuum states and the 0^+ and 1^- components, have been carefully examined by Ogawa and Matsumoto in Ref. [25].

V. $p + {}^8\text{He}$ SCATTERING

A. MCC+AMD results for $p + {}^8\text{He}$ cross sections

In the same way as the 2ch(MCC) calculation of $p + {}^6\text{He}$, the $p + {}^8\text{He}$ reaction at incident energies $E = 15.7, 32.5,$ and 72 MeV/A was calculated by the 2ch(MCC) calculation including the ${}^8\text{He}(0_1^+)$ and ${}^8\text{He}(2_1^+)$ states using the AMDm56 and AMDv58 densities as in the 2ch(MCC) calculation of $p + {}^6\text{He}$. In addition to the 2ch(MCC) calculation, a DWBA calculation of $p + {}^8\text{He}$ was performed to obtain the one-step cross sections.

In Fig. 6(a), the calculated $p + {}^8\text{He}$ elastic cross sections are compared with the data observed in the inverse kinematics experiments [19, 57, 58]. It should again be noted that the deep dip structure of the present result could be smeared by the spin-orbit interaction, which was omitted

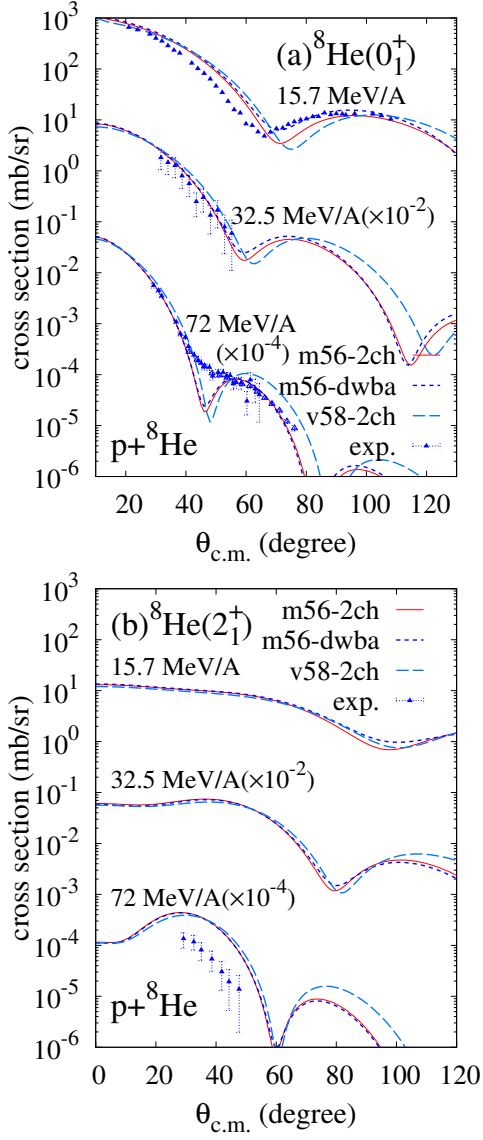


FIG. 6: Calculated ${}^8\text{He}(0_1^+)$ and ${}^8\text{He}(2_1^+)$ cross sections of the $p+{}^8\text{He}$ scattering at $E = 15.7$ MeV/A, 32.5 MeV/A ($\times 10^{-2}$), and 72 MeV/A ($\times 10^{-4}$), and the experimental data from Refs. [19, 57, 58]. The 2ch(MCC) calculations with AMDm56 and AMDv58 and the DWBA calculation with AMDm56 are shown.

in the calculation. Compared with AMDv58, the MCC calculation with AMDm56 obtained a better result for the (p, p) cross sections at $E = 72$ MeV/A for the first- and second-peak amplitudes of the data because of the remarkable neutron skin structure. It also successfully reproduced the data at $E = 32.5$ MeV/A. For the very low-energy data at $E = 15.7$ MeV/A, the AMDm56 result was better than the AMDv58 result, but its reproduction of the data was not satisfactory. This can be understood to be an effect of the lower reliability of the folding model approach for low-energy scattering. In comparison with

the DWBA (one-step) cross sections, the CC effect was negligibly small at $E = 72$ MeV/A but was significant at $E = 15.7$ MeV/A, and the MCC result appeared to be worse than the DWBA result around the second peak. This could suggest a weaker $0_1^+-2_1^+$ coupling than the AMD prediction, but it can not be definitively concluded because the applicability of the present reaction approach to such low-energy p scattering has not been well-tested.

With respect to the (p, p') cross sections to the ${}^8\text{He}(2_1^+)$ state, which are shown in Fig. 6(b), the observed data existed only at $E = 72$ MeV/A [57]. The MCC calculations with AMDm56 and AMDv58 considerably overshoot the experimental data by a factor of three around the peak position.

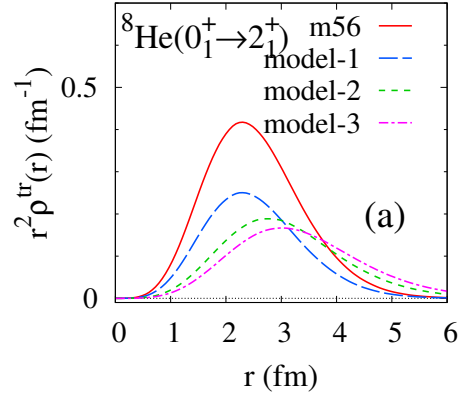


FIG. 7: The neutron transition density of ${}^8\text{He}$ of model functions ($\rho_{n,\text{model-1}}^{\text{tr}}(r)$, $\rho_{n,\text{model-2}}^{\text{tr}}(r)$, and $\rho_{n,\text{model-3}}^{\text{tr}}(r)$) for the $0_1^+ \rightarrow 2_1^+$ transition compared with the original AMDm56 density. The r^2 -weighted transition densities are plotted. The neutron transition matrix element $M_n = 7.6$ fm 2 for the original AMDm56 density was scaled to be $M_n = 4.5$, 5.3 , and 6.1 fm 2 for the model-1, model-2, and model-3 transition densities, respectively.

B. Model analysis of ${}^8\text{He}(2_1^+)$ cross sections

As previously described, the present MCC+AMD calculation overshoot the experimental 2_1^+ cross sections of the $p + {}^8\text{He}$ reaction at $E = 72$ MeV/A by a factor of three. A similar overshooting problem for ${}^8\text{He}(2_1^+)$ cross sections was encountered in the JLM reaction calculation using the NCSM density of ${}^8\text{He}$ in Ref. [23], in which the results were overestimated by a factor of five. Even though the data at $E = 72$ MeV/A contained sizable errors, a significant modification of the predicted neutron transition density could be used to correct the description of the (p, p') data.

We here consider modifications of the theoretical neutron transition density by hand and perform a model analysis to adjust the (p, p') data. For the modifications, we introduced a model function $\rho_{n,\text{model}}^{\text{tr}}(r)$ for the neutron transition density by artificially scaling the original

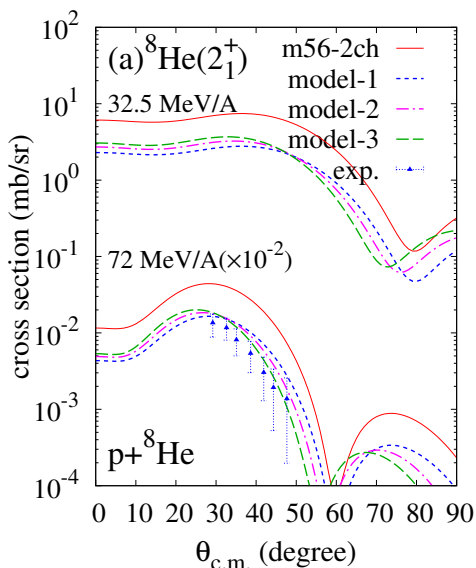


FIG. 8: Cross sections of the $p + {}^8\text{He}$ scattering calculated using the 2ch(MCC) calculations with the model neutron transition densities of $\rho_{n,\text{model-1}}^{\text{tr}}(r)$, $\rho_{n,\text{model-2}}^{\text{tr}}(r)$, and $\rho_{n,\text{model-3}}^{\text{tr}}(r)$. The calculated ${}^8\text{He}(2_1^+)$ cross sections at $E = 32.5$ MeV/A and 72 MeV/A ($\times 10^{-2}$) are compared with the original AMDm56 result and the experimental data from Ref. [57].

AMDm56 density $\rho_{n,m56}^{\text{tr}}(r)$ as follows:

$$\rho_{n,\text{model}}^{\text{tr}}(r) \equiv \frac{f}{a^5} \rho_{n,m56}^{\text{tr}}(r/a). \quad (1)$$

Here, a is the radial scaling factor and f is the overall scaling factor. For this model function, the neutron transition matrix element $M_{n,m56} = 7.6 \text{ fm}^2$ of the original AMDm56 value was scaled to be $M_n = fM_{n,m56}$. For the present analysis, we prepared three types of model transition density, $\rho_{n,\text{model-1,2,3}}^{\text{tr}}(r)$. Model-1 was a transition density $\rho_{n,\text{model-1}}^{\text{tr}}(r) = f\rho_{n,m56}^{\text{tr}}(r)$ simply renormalized from the original transition density using $a = 1$ (no radial scaling). Model-2 and model-3 were obtained by stretching the spatial distribution with radial scaling factors of $a = 1.1$ and $a = 1.2$, respectively. We chose the overall factors $f_1 = 0.6$, $f_2 = 0.7$, and $f_3 = 0.8$ for model-1, model-2, and model-3, respectively, to roughly fit the upper limit of the (p, p') data at $\theta = 32^\circ$. As a result, these phenomenological model transition densities $\rho_{n,\text{model-1}}^{\text{tr}}(r)$, $\rho_{n,\text{model-2}}^{\text{tr}}(r)$, and $\rho_{n,\text{model-3}}^{\text{tr}}(r)$ gave the values $M_n = 4.5$, 5.3 , and 6.1 fm^2 , respectively, which can be regarded as upper limits to reproduce the (p, p') data in each model. Figure 7 shows the neutron transition density of three models.

Using the model neutron transition densities $\rho_{n,\text{model-1}}^{\text{tr}}(r)$, $\rho_{n,\text{model-2}}^{\text{tr}}(r)$, and $\rho_{n,\text{model-3}}^{\text{tr}}(r)$ of the $0_1^+ \rightarrow 2_1^+$ transition, we performed the coupled-channel calculation of the $p + {}^8\text{He}$ reaction using the Melbourne g -matrix folding approach. We did not change other

inputs from the original AMDm56 densities, such as the diagonal and $2_1^+ \rightarrow 2_1^+$ transition densities and the proton component of the $0_1^+ \rightarrow 2_1^+$ transition density.

Figure 8 shows the (p, p') cross sections to the ${}^8\text{He}(2_1^+)$ state at $E = 32.5$ and 72 MeV/A obtained using the three models compared with the experimental data and the original AMDm56 cross sections. As mentioned above, the transition density was renormalized by an overall factor to reproduce the upper limit of the experimental cross sections. For the angle dependence of the (p, p') cross sections, the three models each gave different results. Compared with the experimental (p, p') data, the agreement seems to have been better in the model-2 and model-3 results compared with the model-1 results. This means that a distribution of the neutron transition density broader than the original one was favored. If we renormalized the neutron transition density of model-2 and model-3 to fit the lower limit of the (p, p') data at $\theta = 32^\circ$, we obtained the neutron transition matrix elements of 3.9 and 4.5 fm^2 , respectively, instead of the values 5.3 (model-2) and 6.1 fm^2 (model-3) for the upper limit. Considering these uncertainties, the optimal neutron matrix element to describe the (p, p') data at $E = 72$ MeV/A is likely to be in the range of $M_n = 4\text{--}6 \text{ fm}^2$.

VI. $p + {}^8\text{He}$ AND $\alpha + {}^8\text{He}$ INELASTIC SCATTERING

To investigate the p and α inelastic scattering off ${}^8\text{He}$, we performed MCC+AMD calculations of the $p + {}^8\text{He}$ and $\alpha + {}^8\text{He}$ reactions. These calculations included the $0_{1,2}^+$, 1_1^- , $2_{1,2,3}^+$, and 3_1^- states (seven states in total; called “7ch(MCC)”) and all the $\lambda = 0, 1, 2, 3$ transitions with the AMDm56 densities. As seen in the calculated M_n/M_p ratios shown in Table II, the inelastic transitions from the 0_1^+ state to the 0_2^+ , 1_1^- , 2_3^+ , and 3_1^- states had a remarkable neutron-dominant nature. The proton and neutron components of the AMDm56 transition densities are shown in Fig. 9. The neutron component of the $0_1^+ \rightarrow 0_2^+$ and $0_1^+ \rightarrow 1_1^-$ transition densities showed nodal structures as are usually seen in the isoscalar monopole and dipole transitions of $Z = N$ nuclei. The $0_1^+ \rightarrow 3_1^-$ neutron transition density had a single-peak structure, whereas the $0_1^+ \rightarrow 2_3^+$ neutron transition density had a nodal structure different from the $0_1^+ \rightarrow 2_1^+$ transition with the simple peak.

Figure 10 shows the elastic and 2_1^+ cross sections of the $\alpha + {}^8\text{He}$ reaction at $E = 26$ and 72 MeV/A obtained using the 7ch(MCC) calculation with the AMDm56 densities together with the experimental elastic cross sections at $E = 26$ MeV/A [14, 15]. The MCC calculation successfully reproduced the observed (α, α) data. In comparison with the DWBA (one-step) cross sections, the CC effect had a minor contribution to the ${}^8\text{He}(0_1^+)$ and ${}^8\text{He}(2_1^+)$ cross sections of the $\alpha + {}^8\text{He}$ scattering except for in the case of elastic scattering at backward angles.

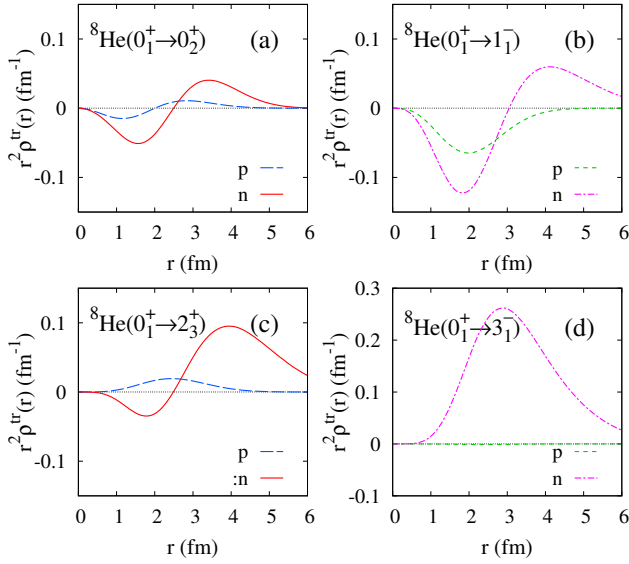


FIG. 9: Proton and neutron transition densities from the ${}^8\text{He}(0_1^+)$ state to the ${}^8\text{He}(0_2^+)$, ${}^8\text{He}(1_1^-)$, ${}^8\text{He}(2_3^+)$ and ${}^8\text{He}(3_1^-)$ states.

The MCC+AMD results of the 0_2^+ , 1_1^- , 2_3^+ , and 3_1^- cross sections of the $p + {}^8\text{He}$ and $\alpha + {}^8\text{He}$ reactions are shown in Fig. 11. According to the AMDm56 prediction, the ${}^8\text{He}(0_2^+)$, ${}^8\text{He}(1_1^-)$, and ${}^8\text{He}(3_1^-)$ states had few MeV energy differences. For experimental search for these states with (p, p') and (α, α') reactions, the production rate and selectivity of each state should be carefully considered. In particular, the (p, p') reaction may be favored to observe the ${}^8\text{He}(3_1^-)$ state because of its high production rate for a wide range of angles. At the same time, the (α, α') reaction had a high selectivity for the ${}^8\text{He}(0_2^+)$ state at forward angles ($\theta_{c.m.} \leq 2^\circ$). For the ${}^8\text{He}(1_1^-)$ state, the dominant contribution was predicted in the (α, α') cross sections around $\theta_{c.m.} \sim 5^\circ$ and at a lower energy of $E = 26 \text{ MeV/A}$.

To see the CC effect in the $p + {}^8\text{He}$ and $\alpha + {}^8\text{He}$ reactions, the DWBA (one-step) cross sections were compared with the MCC calculations (Fig. 12). Because of the strong $0_2^+ \rightarrow 2_3^+$ coupling, a significant CC effect can be observed in the (p, p') cross sections to the ${}^8\text{He}(0_2^+)$ state and the (α, α') cross sections to the ${}^8\text{He}(0_2^+)$ and ${}^8\text{He}(2_3^+)$ states, for the low energy reactions in particular.

The relative high productions of the ${}^8\text{He}(0_2^+)$ and ${}^8\text{He}(1_1^-)$ states in the (α, α') reaction compared with the (p, p') reaction can be understood in terms of the nodal behavior of the transition density. In general, the (α, α') reaction is a sensitive probe to the transition density at the surface and outer regions because of the strong absorption of the α -nucleus potentials in the interior region. As mentioned earlier the neutron transition densities from the ground to the ${}^8\text{He}(0_2^+)$ and ${}^8\text{He}(1_1^-)$ states had a remarkable amplitude in the outer region (Figs. 9(a) and (b)), and this outer amplitude predominantly contributed to the (α, α') cross sections. At the

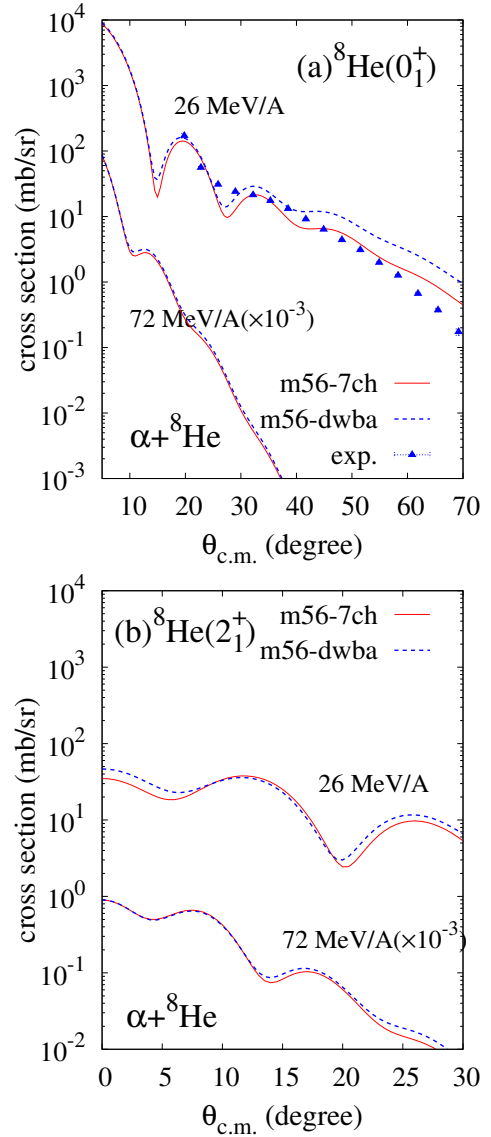


FIG. 10: Calculated ${}^8\text{He}(0_1^+)$ and ${}^8\text{He}(2_1^+)$ cross sections of the $\alpha + {}^8\text{He}$ reaction at $E = 26 \text{ MeV/A}$ and $72 \text{ MeV/A} (\times 10^{-2})$ obtained by the 7ch(MCC) and DWBA calculations with the AMDm56 densities. The experimental data of the elastic cross sections at $E = 26 \text{ MeV/A}$ from Refs. [14, 15] are also shown.

same time, in the p scattering with a weaker absorption, the inner amplitude had a negative contribution and canceled out the contribution of the outer amplitude and suppressed the forward angle cross sections. High productions of the monopole and dipole transitions by (α, α') reactions have been observed for isoscalar transitions in $Z \approx N$ nuclei. The new finding obtained here is that a similar trend was also predicted in neutron-dominant transitions in neutron-rich nuclei.

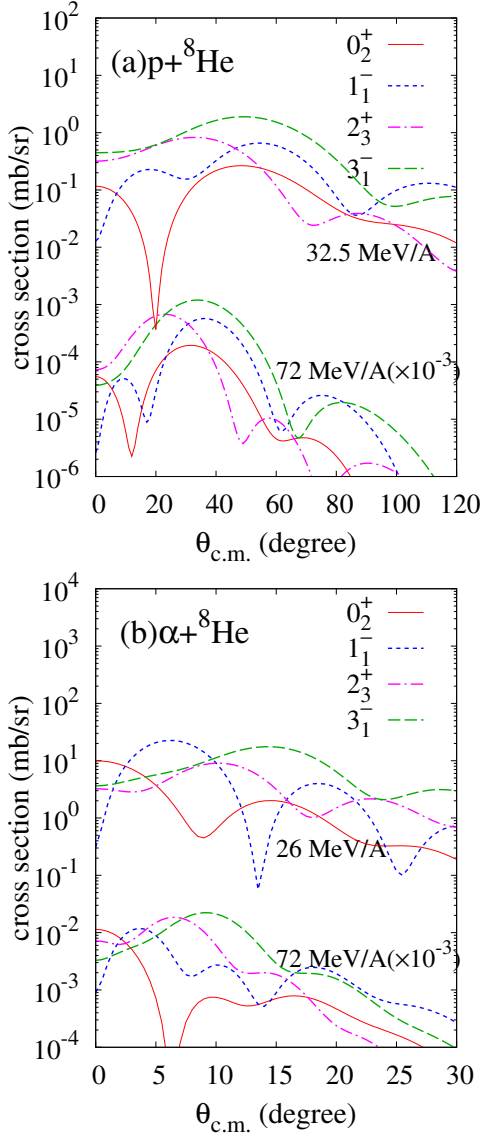


FIG. 11: Calculated (p, p') cross sections at $E = 32.5 \text{ MeV/A}$ and $72 \text{ MeV/A} (\times 10^{-2})$ and (α, α') cross sections at $E = 26 \text{ MeV/A}$ and $72 \text{ MeV/A} (\times 10^{-2})$ to the ${}^8\text{He}(0_2^+)$, ${}^8\text{He}(1_1^-)$, ${}^8\text{He}(2_3^+)$, and ${}^8\text{He}(3_1^-)$ states obtained by the 7ch(MCC) calculations with the AMDm56 densities.

VII. SUMMARY

The elastic and inelastic cross sections of the $p + {}^6\text{He}$, $p + {}^8\text{He}$, and $\alpha + {}^8\text{He}$ reactions were investigated using the Melbourne g -matrix folding approach. In the reaction calculations, the transition and coupling potentials of nucleon–nucleus systems were microscopically obtained by folding the Melbourne g -matrix NN interaction with the diagonal and transition densities of the target nucleus, and the α –nucleus potentials were calculated by folding the nucleon–nucleus potentials with the α density. The theoretical densities obtained us-

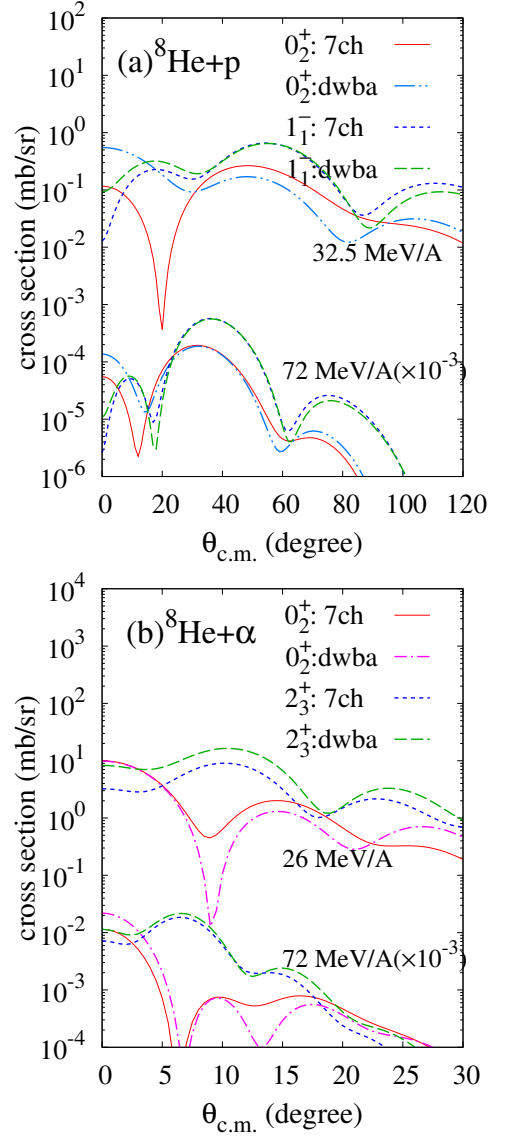


FIG. 12: DWBA cross sections of the $p + {}^8\text{He}$ reaction at $E = 32.5 \text{ MeV/A}$ and $72 \text{ MeV/A} (\times 10^{-2})$ and of the $\alpha + {}^8\text{He}$ reaction at $E = 26 \text{ MeV/A}$ and $72 \text{ MeV/A} (\times 10^{-2})$ to the ${}^8\text{He}(0_2^+)$ and ${}^8\text{He}(1_1^-)$ states compared with the 7ch(MCC) calculations.

ing the microscopic structure model of AMD were used for the MCC calculations of the $p + {}^6\text{He}$, $p + {}^8\text{He}$, and $\alpha + {}^8\text{He}$ reactions. One of the unique characteristics of the present work using MCC+AMD is that we investigated the $p + {}^6\text{He}$, $p + {}^8\text{He}$, and $\alpha + {}^8\text{He}$ reactions on the same footing in the microscopic framework. We first demonstrated the success of the MCC+AMD calculation in reproducing elastic cross sections, and then discussed the transition properties of the ${}^6\text{He}(2_1^+)$ and ${}^8\text{He}(2_1^+)$ states with detailed analyses of the (p, p') cross sections. It should be stressed that the Melbourne g -matrix folding approach has no adjustable parameters differently from

phenomenological reaction analysis. This is a great advantage to test the reliability of structure model inputs via the cross section data.

For the $p + {}^6\text{He}$ and $p + {}^8\text{He}$ elastic scattering, the present MCC+AMD calculation reproduced well the $p + {}^6\text{He}$ cross sections at $E=40.9$ MeV/A and the $p + {}^8\text{He}$ cross sections at $E = 32.5$ and 72 MeV/A.

For the $p + {}^6\text{He}$ inelastic scattering to the ${}^6\text{He}(2_1^+)$ state at $E = 24.5$, and 40.9 MeV/A, the MCC+AMD results demonstrated a reasonable reproduction of the peak amplitude, supporting the predicted value of $M_n = 7.9$ fm². However, the result was not satisfactory in describing the angle dependence of the (p, p') data in detail. We performed a model analysis using the Melbourne g -matrix folding approach with phenomenological halo-type densities and demonstrated that a better reproduction can be obtained using a broader neutron transition density than that in the AMD prediction.

For the ${}^8\text{He}(2_1^+)$ cross sections of the $p + {}^8\text{He}$ reaction, the present MCC+AMD calculation considerably overshoot the (p, p') data at $E = 72$ MeV/A by a factor of three. This overshooting was consistent with the reaction analysis with the NCSM density performed in Ref. [23]. To gather information concerning the neutron transition from the (p, p') data, we performed a further model analysis by introducing phenomenological modifications of the neutron component of the $0_1^+ \rightarrow 2_1^+$ transition density to fit the (p, p') data at $E = 72$ MeV/A, and obtained a plausible value of $M_n = 4-6$ fm², which was smaller than that obtained by the AMD predictions ($M_n = 6.4-7.6$ fm²). For a more detailed discussion on this point, high-quality data for a wide energy range would be required.

For p scattering below $E = 25$ MeV/A, the present results were not satisfactory in precisely reproducing the

observed $p + {}^6\text{He}$ and $p + {}^8\text{He}$ elastic cross sections. The applicability of the present reaction approach to such the low-energy p scattering should be carefully examined. For example, the validity of the local density approximation treatment for light-mass nuclei with large isospin asymmetry remains to be checked. Coupling with continuum states may also contribute to the low-energy p scattering off loosely bound nuclei.

For the $\alpha + {}^8\text{He}$ reaction, the MCC+AMD calculation reproduced the observed (α, α) cross sections at $E = 26$ MeV/A. The theoretical predictions of the (p, p') and (α, α') cross sections to higher excited states of ${}^8\text{He}$ were presented, and the production rates in the $p + {}^8\text{He}$ and $\alpha + {}^8\text{He}$ inelastic scattering were discussed. It was suggested that the (p, p') reaction was favored for the ${}^8\text{He}(3_1^-)$ observation, whereas the (α, α') reaction at forward angles sensitively probed the ${}^8\text{He}(0_2^+)$ and ${}^8\text{He}(1_1^-)$ states. Our results indicate that α inelastic scattering has the potential to be a good probe for neutron-dominant monopole and dipole excitations, and its wide application to neutron-rich nuclei is expected in future experiments in inverse kinematics.

Acknowledgments

The authors would like to thank Dr. Matsumoto and Mr. Ogawa for their fruitful discussions. The computational calculations of this work were performed using the supercomputer at the Yukawa Institute for Theoretical Physics at Kyoto University. The work was supported by Grants-in-Aid of the Japan Society for the Promotion of Science (Grant Nos. JP18K03617, JP16K05352, and 18H05407) and by a grant of the joint research project of the Research Center for Nuclear Physics at Osaka University.

-
- [1] M.N. Harakeh, A. van der Woude, Giant Resonances, Oxford University Press, 2001.
 - [2] K. Van Der Borg, M. N. Harakeh and A. Van Der Woude, Nucl. Phys. A **365**, 243 (1981).
 - [3] D. H. Youngblood, H. L. Clark and Y.-W. Lui, Phys. Rev. Lett. **82**, 691 (1999).
 - [4] M. Uchida *et al.*, Phys. Rev. C **69**, 051301 (2004).
 - [5] A. M. Bernstein, V. R. Brown and V. A. Madsen, Phys. Lett. **71B**, 48 (1977).
 - [6] A. M. Bernstein, V. R. Brown and V. A. Madsen, Phys. Rev. Lett. **42**, 425 (1979).
 - [7] A. M. Bernstein, V. R. Brown and V. A. Madsen, Phys. Lett. **103B**, 255 (1981).
 - [8] B. A. Brown and B. H. Wildenthal, Phys. Rev. C **21**, 2107 (1980).
 - [9] B. A. Brown *et al.*, Phys. Rev. C **26**, 2247 (1982).
 - [10] T. Wakasa *et al.*, Phys. Lett. B **653**, 173 (2007).
 - [11] M. Itoh *et al.*, Phys. Rev. C **84**, 054308 (2011).
 - [12] T. Kawabata *et al.*, Few Body Syst. **54**, 93 (2013).
 - [13] S. Adachi *et al.*, Phys. Rev. C **97**, no. 1, 014601 (2018).
 - [14] R. Wolski *et al.*, Nucl. Phys. A **701**, 29 (2002).
 - [15] R. Wolski *et al.*, Nucl. Phys. A **722**, C55 (2003).
 - [16] T. Furuno *et al.*, Phys. Rev. C **100**, no. 5, 054322 (2019).
 - [17] J. P. Jeukenne, A. Lejeune and C. Mahaux, Phys. Rev. C **16**, 80 (1977).
 - [18] V. Lapoux *et al.*, Phys. Lett. B **517**, 18 (2001).
 - [19] F. Skaza *et al.*, Phys. Lett. B **619**, 82 (2005). doi:10.1016/j.physletb.2005.05.061
 - [20] C. Jouanne *et al.*, Phys. Rev. C **72**, 014308 (2005).
 - [21] M. Takashina, Y. Kanada-En'yo and Y. Sakuragi, Phys. Rev. C **71**, 054602 (2005).
 - [22] M. Takashina and Y. Kanada-En'yo, Phys. Rev. C **77**, 014604 (2008).
 - [23] V. Lapoux and N. Alamanos, Eur. Phys. J. A **51**, no. 7, 91 (2015).
 - [24] T. Matsumoto, J. Tanaka and K. Ogata, PTEP **2019**, no.12, 123D02 (2019).
 - [25] S. Ogawa and T. Matsumoto, [arXiv:2003.05123 [nucl-th]].
 - [26] K. Amos, P. J. Dortmans, H. V. von Geramb, S. Karataglidis, and J. Raynal, Adv. Nucl. Phys. **25**, 275 (2000).

- [27] A. Lagoyannis *et al.*, Phys. Lett. B **518**, 27 (2001).
- [28] S. V. Stepanov *et al.*, Phys. Lett. B **542**, 35 (2002).
- [29] S. Karataglidis, Y. J. Kim and K. Amos, Nucl. Phys. A **793**, 40 (2007).
- [30] K. Minomo, K. Ogata, M. Kohno, Y. R. Shimizu and M. Yahiro, J. Phys. G **37**, 085011 (2010).
- [31] M. Toyokawa, K. Minomo and M. Yahiro, Phys. Rev. C **88**, no. 5, 054602 (2013).
- [32] K. Egashira, K. Minomo, M. Toyokawa, T. Matsumoto and M. Yahiro, Phys. Rev. C **89**, 064611 (2014).
- [33] K. Minomo and K. Ogata, Phys. Rev. C **93**, 051601 (2016).
- [34] K. Minomo, K. Washiyama and K. Ogata, arXiv:1712.10121 [nucl-th].
- [35] Y. Kanada-En'yo and K. Ogata, Phys. Rev. C **99**, no. 6, 064601 (2019).
- [36] Y. Kanada-En'yo and K. Ogata, arXiv:1904.03811 [nucl-th].
- [37] Y. Kanada-En'yo and K. Ogata, Phys. Rev. C **100**, no. 6, 064616 (2019).
- [38] Y. Kanada-En'yo and K. Ogata, arXiv:2002.02625 [nucl-th].
- [39] Y. Kanada-En'yo, H. Horiuchi and A. Ono, Phys. Rev. C **52**, 628 (1995).
- [40] Y. Kanada-En'yo and H. Horiuchi, Phys. Rev. C **52**, 647 (1995).
- [41] Y. Kanada-En'yo, M. Kimura and A. Ono, PTEP **2012** 01A202 (2012).
- [42] A. K. Kerman, H. McManus, and R. M. Thaler, Ann. Phys. **8**, 551 (1959).
- [43] R. Machleidt, K. Holinde and C. Elster, Phys. Rept. **149**, 1-89 (1987).
- [44] Y. Kanada-En'yo, Phys. Rev. C **76**, 044323 (2007).
- [45] L.-B. Wang *et al.*, Phys. Rev. Lett. **93**, 142501 (2004).
- [46] P. Mueller *et al.*, Phys. Rev. Lett. **99**, 252501 (2007).
- [47] I. Tanihata, D. Hirata, T. Kobayashi, S. Shimoura, K. Sugimoto and H. Toki, Phys. Lett. B **289**, 261 (1992).
- [48] A. Ozawa, T. Suzuki and I. Tanihata, Nucl. Phys. A **693**, 32 (2001).
- [49] D. R. Tilley, C. M. Cheves, J. L. Godwin, G. M. Hale, H. M. Hofmann, J. H. Kelley, C. G. Sheu and H. R. Weller, Nucl. Phys. A **708**, 3 (2002).
- [50] D. R. Tilley, J. H. Kelley, J. L. Godwin, D. J. Millener, J. E. Purcell, C. G. Sheu and H. R. Weller, Nucl. Phys. A **745**, 155 (2004).
- [51] K. Varga, Y. Suzuki and Y. Ohbayasi, Phys. Rev. C **50**, 189 (1994).
- [52] E. Caurier and P. Navratil, Phys. Rev. C **73**, 021302 (2006).
- [53] P. Navratil and W. E. Ormand, Phys. Rev. Lett. **88**, 152502 (2002).
- [54] P. Navratil and W. E. Ormand, Phys. Rev. C **68**, 034305 (2003).
- [55] L. Giot, P. Roussel-Chomaz, C. Demonchy, W. Mitig, H. Savajols, N. Alamanos, F. Auger, A. Gillibert, C. Jouanne, V. Lapaoux, L. Nalpas, E. Polacco, J. Sida, F. Skaza, M. Cortina-Gil, J. Fernandez-Vasquez, R. Mackintosh, A. Pakou, S. Pita, A. Rodin, S. Stepantsov, T. Akopian, G.M., K. Rusek, I. Thompson and R. Wolski, Phys. Rev. C **71**, 064311 (2005).
- [56] R. Wolski *et al.*, Phys. Lett. B **467**, 8 (1999).
- [57] A. A. Korshennikov *et al.*, Phys. Lett. B **316**, 38 (1993).
- [58] A. A. Korshennikov *et al.*, Phys. Lett. B **343**, 53 (1995).